



Supplementary Materials for

Microwave observations reveal the deep extent and structure of Jupiter's atmospheric vortices

S. J. Bolton *et al.*

Corresponding author: S. J. Bolton, sbolton@swri.edu

Science **374**, 968 (2021)
DOI: [10.1126/science.abf1015](https://doi.org/10.1126/science.abf1015)

The PDF file includes:

Materials and Methods
Supplementary Text
Figs. S1 to S7
Tables S1 to S5
References

Materials and Methods

Estimation of signal strength

The MWR data set shown in Figure 1 is comprised of samples every few tenths of a degree in longitude (varying over the map) and approximately every 1.5 degrees in latitude. A screening algorithm was used to remove observations significantly contaminated by synchrotron emission. However, this did not result in removal of data from our data set because synchrotron emission contamination is only important for observations when the antenna beam is not completely on the planet or for observations at latitudes poleward of $\sim 60^\circ\text{N}$ (7,9). The thermal emission brightness temperatures, T_b , are then deconvolved from the antenna temperatures taking into consideration the antenna beam pattern including potential synchrotron contamination in the side lobes (7,9). Figure S1 shows the half-power beam width resolution for MWR (at 10 GHz), indicating the resolution of the maps in Figure 1.

For the 38°N feature, frequencies at and above 1.25 GHz, observed at $\sim 36.6^\circ\text{N}$, 38.1°N and $\sim 39.7^\circ\text{N}$ bracketing a feature with a peak observed in the 38.1°N scan (Fig. 1). The latitude above this observed peak shows the feature flips to the opposite sense (colder vs warmer depending on frequency observed). At 0.6 GHz, the antenna is mounted on a different side of the spacecraft from the other MWR antennas, and thus samples the planet one third of a spin (10 seconds) later than the other frequencies, observing a slightly different latitude due to the spacecraft motion. The scans at 0.6 GHz are at 37.1°N , 38.7°N and 40.2°N . The signature at 38.7°N is greater than in the adjacent scans. The scan at about 40.2°N shows an increase in T_b in contrast to the decrease at 38.7°N . This characteristic is consistent with what is seen at other frequencies. The contrast with adjacent scans, combined with the signature at other frequencies in the same location, despite different latitude sampling, indicates that the signature at 0.6 GHz is associated with the same feature seen at other frequencies. We conclude that it is neither an artifact nor a coincidental fluctuation.

To analyze the two features at 19°N and 38°N we selected regions to use as the background by extracting T_b from scans surrounding the features from nearby latitude and longitudes $\pm\sim 20^\circ$. From this selected data set, we define a quiet region to be used as background outside the regions exhibiting perturbations related to the two features, then normalized all T_b measurements to this background. For the 19°N feature the background corresponded to longitudes in System III coordinates (36) of 102°W to 107°W . For the 38°N feature the background corresponded to System-III longitudes from 90°W to 95°W . We de-trended the signal for the 1.25 GHz and 0.6 GHz frequencies as a function of longitude using a degree-5 polynomial, dividing the T_b variations obtained at each MWR frequency by their median value to obtain an estimate of the T_b variation for each feature in each channel. The normalized, detrended data are plotted for the six MWR frequencies as a function of longitude and latitude in Fig. S2.

The 19°N anticyclone is identified in Figure S2A-F with a decrease in T_b of about 2% at 22 GHz, 3.5% at 10 and 5.2 GHz and about 1% at 2.6 GHz. It is not detected at the two lowest frequencies. The 38°N feature is identified in Figure S2G-L with the cyclone elongated in longitude, and well-defined in latitude. Unlike the 19°N anticyclone, the 38°N feature appears warmer at 5.6 GHz and above, and colder at frequencies below 5.6 GHz.

To quantify the depth of the features and assess corresponding uncertainties, we selected points at the center and outside of the features, both at different longitudes with similar latitudes and at different latitudes with similar longitudes. We compare the variations in T_b for these three ensembles of points in Figure S3. For the 19°N feature, the values of the background points are similar but with a larger spread for the points at the same longitude, a consequence of the anticyclone character and its perturbation of the surrounding zonal flow. Focusing on the difference between the center of the anticyclones and the points in a quiet region at longitudes 102°W to 105°W, Figure S3 reveals a decrease in T_b at frequencies at 2.6 GHz and above. The signal is lower than the background at 0.6 GHz and 1.2 GHz. We estimate the uncertainties by adding the standard deviations quadratically. The resulting change in T_b in all six MWR frequencies is listed in Table S1.

For the 38°N cyclone one ensemble of points inside the cyclone and two ensembles of points outside the cyclone were selected at different latitudes and different longitudes. As seen in Figure S3, these two ensembles of control points have very similar properties. The T_b variations of the 38°N cyclone are listed in Table S2.

For a comparison with the GRS, we select the 18°S latitude, which is characterized by an inversion in the brightness temperature variation compared to the background. Data obtained at PJ7 for the GRS structure was compared to the background signal at that latitude by calculating the median of the brightness temperatures obtained for PJ1,3,4,5,6,8 and 9. The offset due to the GRS was calculated from the difference between these values. The corresponding uncertainty was estimated from the standard deviation of the background during the multiple perijoves (except PJ7). The results are listed in Table S3. The GRS is a very old, extended and complex vortex. We focus on a representative region of the anticyclone, however other latitudes do not show a similar inversion in the brightness temperature. This implies powerful circulation inside the vortex.

Tables S1 to S3 list brightness temperature anomalies for the 6 MWR frequencies of each vortex, compared to the background longitudinal averages. These data characterize the vortices, not the zonal flow.

Analysis of vortex structure and depth

In the microwave regime, the flux emitted by an atmosphere with a temperature profile $T(z)$ can be approximated by

$$T_b = \int T e^{-\tau} \alpha dz, \quad (s1)$$

where $\tau = \int_z^{z_0} \alpha dz'$ is the optical depth, α the absorption coefficient for the wavelength considered, and z the altitude (2:7). This approximation is accurate to a precision of $\sim hc/(\lambda kT)$, which is $\sim 10^{-3}$ for a temperature $T=300$ K and a wavelength of $\lambda=5$ cm, and valid in the one dimensional approximation, The contribution function $C(z)$ is defined such that

$$T_b = \int C(z) d \ln P, \quad (s2)$$

i.e.,

$$C(z) = Z e^{-\tau} \alpha \frac{RT^2}{\mu g}, \quad (\text{s3})$$

where Z is the gas compressibility factor, R the gas constant, μ the mean molecular weight, g the planet's gravitational acceleration, assuming hydrostatic equilibrium.

We seek to determine how perturbations from a known temperature or ammonia abundance (thus absorption) profile may affect the measured brightness temperature in a given MWR channel.

We first consider a perturbation in temperature, T' , such that $T' = (1 + \delta_T)T$, with $\delta_T \ll 1$, and assume that the absorption profile is unchanged. In that case, the perturbed contribution function becomes, to first order,

$$C'(z) = Z e^{-\tau} \alpha \frac{RT^2}{\mu g} (1 + 2\delta_T). \quad (\text{s4})$$

The change in brightness temperature $\Delta T_b \equiv T'_b - T_b$ (with T'_b being the brightness temperature associated with the new T' temperature profile) then becomes

$$\Delta T_b = \int C(z) 2\delta_T d \ln P. \quad (\text{s5})$$

A relative change in brightness temperature can thus be associated to a relative change in temperature profile with half the magnitude.

We next consider the case of a perturbation that leaves the temperature profile unchanged but modifies the ammonia abundance, so therefore the absorption profile changes. We also assume that absorption is proportional to the ammonia abundance (an assumption which is valid at most altitudes (2,3:7,9)). Therefore, $\alpha' = (1 + \delta_\alpha)\alpha$, implying

$$C'(z) = Z e^{-\tau'} \alpha \frac{RT^2}{\mu g} (1 + \delta_\alpha). \quad (\text{s6})$$

The perturbed optical depth can be calculated if we further assume that the absorption and δ_x are constant on the scales of interest, i.e., when the values of $C(z)$ are the largest. In that case, $\tau' = \tau(1 + \delta_\alpha)$, implying

$$C'(z) = C(z) e^{-\tau\delta_\alpha} (1 + \delta_\alpha). \quad (\text{s7})$$

Because we are considering levels for which the optical depth is small, we consider that $\tau\delta_\alpha \ll 1$, thus

$$C'(z) \approx C(z) [1 - (\tau - 1)\delta_\alpha]. \quad (\text{s8})$$

The change in brightness temperature associated with a change in absorption is thus

$$\Delta T_b \approx - \int C(z) (\tau - 1) \delta_\alpha d \ln P. \quad (\text{s9})$$

This implies that an increase in absorption leads to a larger contribution to the brightness temperature from levels at low optical depth ($\tau < 1$) and a smaller one from the deeper levels. Because the temperature is increasing with pressure, the second effect dominates and leads to a brightness temperature variation that is inversely proportional to the change in absorption.

In the limit that the changes in temperature and/or ammonia abundance occur on length scales that are long compared to the extent of the weighting functions for the different MWR channels, both effects can be combined by seeking values of δ_x compatible with the measured variations ΔT_b such that

$$\Delta T_b \approx \int C(z) \delta_x d \ln P. \quad (\text{s10})$$

Changes δ_x can then be attributed to changes in temperature, in which case $\delta_T = \delta_x/2$; or to changes in absorption/ammonia abundance, in which case $\delta_\alpha \approx -(\tau_{\text{eff}} - 1)\delta_x$, and τ_{eff} is an effective optical depth, dependent on the channel used.

To estimate the feature structure and depth, we use the contribution functions $C_i(P)$ (with $i=1$ to 6 corresponding to the six MWR frequencies) from Figure S1 to calculate the relative T_b variation $\Delta T_{b,i}/T_{b,i}$ that would arise from a perturbation in opacity or temperature $\delta_x(P)$. From our observations of Jupiter's GRS and from theoretical models of anticyclones (15, 18, 19), we expect $\delta_x(P)$ to change sign in the atmosphere. We therefore parametrize it as a sum of three error functions (erf):

$$\delta_x(P) = \frac{a}{2} \left(1 + \text{erf}(\alpha_0(\log P - x_0)) \right) + \frac{b-a}{2} \left(1 + \text{erf}(\alpha_1(\log P - x_1)) \right) - \frac{b}{2} \left(1 + \text{erf}(\alpha_2(\log P - x_2)) \right) \quad (\text{s11})$$

We then perform a Monte Carlo analysis, varying the parameters $a, b, x_0, x_1, x_2, \alpha_0, \alpha_1, \alpha_2$ until we find values of $\Delta T_{b,i}$ matching those arising from our analysis of the MWR measurements. The parameters are selected randomly with uniform distributions, in the ranges listed in Table S4. To avoid unnecessary calculations, the range of values of parameters a and b differ for each vortex, without affecting the final results. The other parameters are the same for the three vortices.

We seek models that minimize

$$\chi^2 = \frac{1}{6} \left\{ \sum_{i=1,6} \left[\left(\frac{\Delta T_{b,i}}{T_{b,i}} \right)_{\text{calc}} - \left(\frac{\Delta T_{b,i}}{T_{b,i}} \right)_{\text{MWR}} \right]^2 / (\sigma_{\Delta T_{b,i}}/T_{b,i})^2 \right\}^{1/2} \quad (\text{s12})$$

where $\left(\frac{\Delta T_{b,i}}{T_{b,i}} \right)_{\text{MWR}}$ and $\sigma_{\Delta T_{b,i}}/T_{b,i}$ are the relative brightness temperature variation and standard deviations relative to the median $T_{b,i}$, listed in Tables S1 and S2. We retain models for which $\chi^2 \leq 1$.

The contribution functions $C_i(P)$ are obtained assuming an adiabatic temperature profile anchored to 166.1 K at 1 bar, using established methods (7,37) and including the additional opacity provided by alkali metals at 1600 K and higher temperatures. For each feature, we calculate two extreme contribution functions as follows. We use the minimum and maximum NH_3 abundances as a function of pressure (3,9), both for the 19°N and 38°N regions, respectively (see Fig. S4 and S5). For the GRS, we use the profiles obtained around 18°S to calculate an upper and a lower abundance of ammonia as a function of depth that encompasses most of the solutions. The resulting abundances are shown in Fig. S5. We then account for the emission angles of the 19°N and 38°N features, $\sim 20^\circ$ and $\sim 45^\circ$, respectively and assume a nadir observation of the GRS. (As a result, the contribution functions of the 38°N cyclone are shifted towards lower pressures.) The resulting contribution functions are shown in Fig. S6.

Our lowest envelope of ammonia abundances for the GRS pushes the maximum of the contribution function at 0.6 GHz down to great depth (Fig. S6). This is due to an assumed slow increase of the ammonia abundance from 225 ppmv to 350 ppmv between 100 and 1000 bar. However, the maximum depth of the GRS obtained from the Juno gravity observations rules out that the GRS is extending to more than ~ 660 bar, at the 3σ level (22).

Supplementary Text

Comparison of analyses

The results obtained in Fig. 3 for the 19°N and 38°N features are consistent with the results obtained from a full inversion and shown in Fig. S4. Comparing the background atmosphere and the latitudes in the region of the two features in Fig. S4 shows that, for the 19°N anticyclone, the transition from a high to a low ammonia abundance takes place around 5 bar, and the perturbation fades away by about 20-30 bars. The 38°N cyclone has a low ammonia abundance relative to the background at low pressures until it transitions to a high ammonia abundance between 2.5 and 6 bar. For the assumptions used to calculate Fig. S4 (9), the perturbation tails off near 30 bars.

For the GRS, we obtain a transition from a negative to a positive anomaly between 30 and 100 bar, in agreement with the analysis of Juno gravity data (22).

Determining the sign of vorticity of the 19°N and 38°N vortices

No measurements of wind motion are available for these features, so their vorticity is determined indirectly. First, we assume that the features have vorticities that are the same sign as the horizontal wind shear in their environment or they would be destroyed in approximately their rotation period (17). Long-lived Jovian vortices with measured vorticities have the same sign as that of the shear in which they are embedded (15).

Upper-tropospheric low-temperature anomalies can be used to identify cloud features as anticyclonic (16,19). The Great Red Spot was observed as a cold thermal feature by Voyager (25), leading to the suggestion that rising motions and adiabatic cooling are responsible for the cold anomaly. This has been generalized to all anticyclones (18,38) and used to predict the converse outcome: warm upper temperatures occur for cyclones. We therefore expect anticyclones to be cold, humid, cloudy regions in the upper troposphere and cyclones to be warm, dry and clear at

that altitude. We sought verifying observations of temperatures, as well as cloud opacity and the relative abundance of ammonia gas, a condensate, from Juno-supporting mid-infrared observations (39,40).

The closest such observations to PJ19 (6 April 2019) were made a few weeks later on 26 May 2019 using the COMICS instrument at the Subaru Telescope (41). The features at 19°N and 38°N were tracked by the amateur community during that period (39) and are identified in a composite visible image made three days later (Figure S7, panel A). At this time, the dark feature at 38°N has drifted to the east in longitude away from the feature at 19°N. Brightness-temperature maps of this region from the COMICS observations are shown in panels B-D of Figure S7. The 20.5- μm thermal emission is sensitive to physical temperatures near the 300-mbar level in Jupiter's upper troposphere, the 10.3- μm and 8.7- μm emission is sensitive to the distribution of ammonia gas near 300-mbar, above the condensation level, and to the opacity of an ammonia-condensate cloud whose base is near 700 mbar.

The visibly dark feature at 38°N is recognizable as a relatively bright/warm region in panels B-D of Figure S7. It is warmer than its surroundings by $\sim 0.8\text{-}1.0\text{K}$ at 20.5 μm (Fig. S7, panel B), implying an equivalent temperature increase near the 300-mbar level of the upper troposphere. Its relatively bright appearance in at 10.3 μm (panel C) and 8.7 μm (panel D) are consistent with it being a relatively warm and/or ammonia-depleted and aerosol-free region, whose reduced opacity allows radiation to emerge from warmer depths of the atmosphere. These properties are consistent with being cyclonic in nature with prevailing vertical downwelling motions at this level of the atmosphere, confirming conclusions in the main part of this paper. On the other hand, determining whether the compact feature at 19°N is a relatively cold, "humid" and cloudy anticyclone is complicated by the diffraction- and seeing-limited resolution of these images, on the order of $3^\circ\text{-}4^\circ$, which is larger than feature itself. As a result, this feature is unresolved, particularly at 20.5 μm (panel B of Fig. S7), and exacerbated by the presence of the very warm region associated with the North Equatorial Belt (NEB) immediately to its south. The cold "notch" in the warm NEB at 10.3 μm (panel C) would not be inconsistent with the feature having relatively higher ammonia and more opaque cloud layer, but we cannot make any more definitive statement. Inversion of these measurements to retrieve physical properties of the atmosphere for many regions in these maps to compare with MWR results is beyond the scope of this paper, but is to be addressed in future work.

Description of the visible and infrared maps in Figure 1

Infrared and visible maps in Fig. 1 show variation in cloud properties over a limited altitude range, which is complementary to MWR observations of gas density (via ammonia concentration and kinetic temperature) extending to much deeper levels (13,34). The infrared images were acquired by the NIRI instrument at Gemini North Observatory, and the visible images were acquired by the WFC3 instrument on the Hubble Space Telescope. Data acquisition and processing are fully described in (13).

The MWR footprint coordinates were used to crop full global infrared and visible maps to cover the same regions of Jupiter's atmosphere in Fig. 1 of the main paper. Figure 8 in (13) shows the full global map source data.

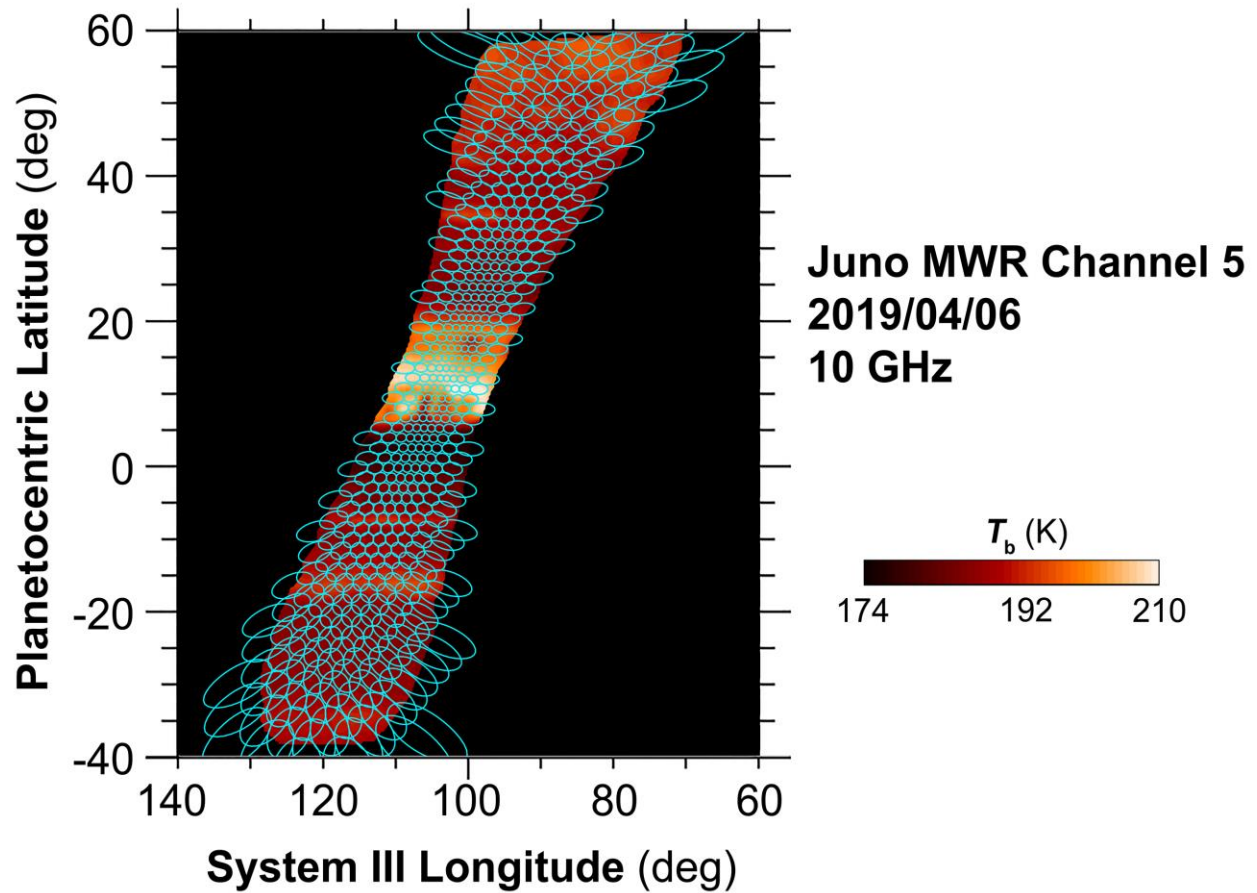


Figure S1. **Half-power beam width resolution for MWR at 10 GHz.** To illustrate the resolution of MWR maps, the microwave beam patterns for 2.4 to 22 GHz channels are shown in blue overlaid on the 10 GHz map of Figure 1. MWR maps at frequencies between 2.4 and 22 GHz have similar resolution. At frequencies of 1.2 GHz and 0.6 GHz, the beam width is approximately twice that shown.

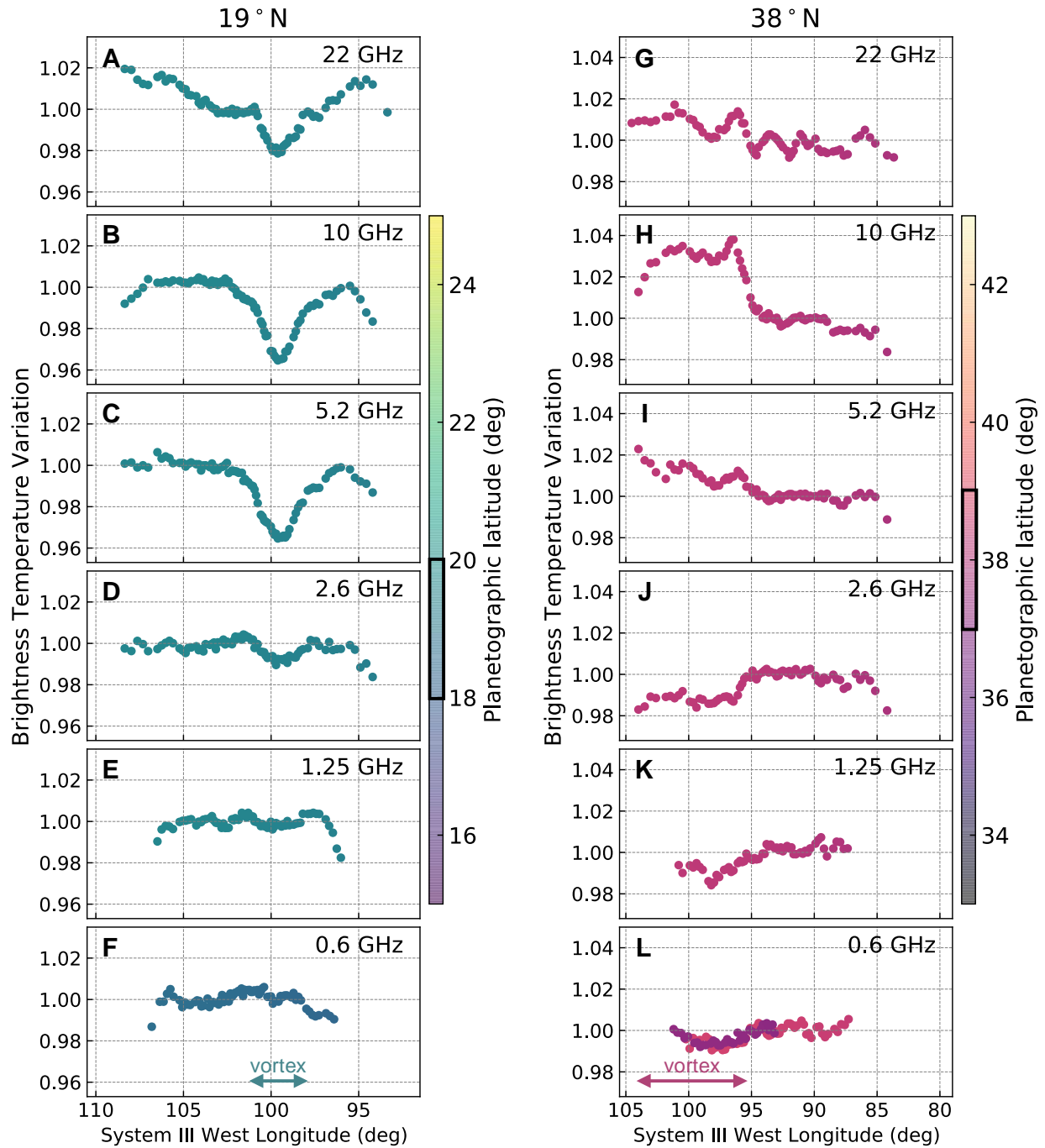


Figure S2. **Brightness temperatures for the 19°N anticyclone and 38°N cyclone.** MWR brightness temperature data points from cross-track data binned by latitude and west longitude for the 19°N anticyclone (A-F) and for the 38°N cyclone (G-L)). Each panel provides a comparison of brightness temperature relative to the background for all MWR frequencies (see values listed in Tables S1 and S2). The different colors represent data corresponding to different latitudes. The color for the Juno tracks intersecting the latitude of the feature (i.e., between 18°N and 20°N for the 19°N feature and between 37°N and 39°N for the 38°N feature) is highlighted by black boxes on the color bars. The location of the vortices in longitude is shown in the bottom panels (F and L).

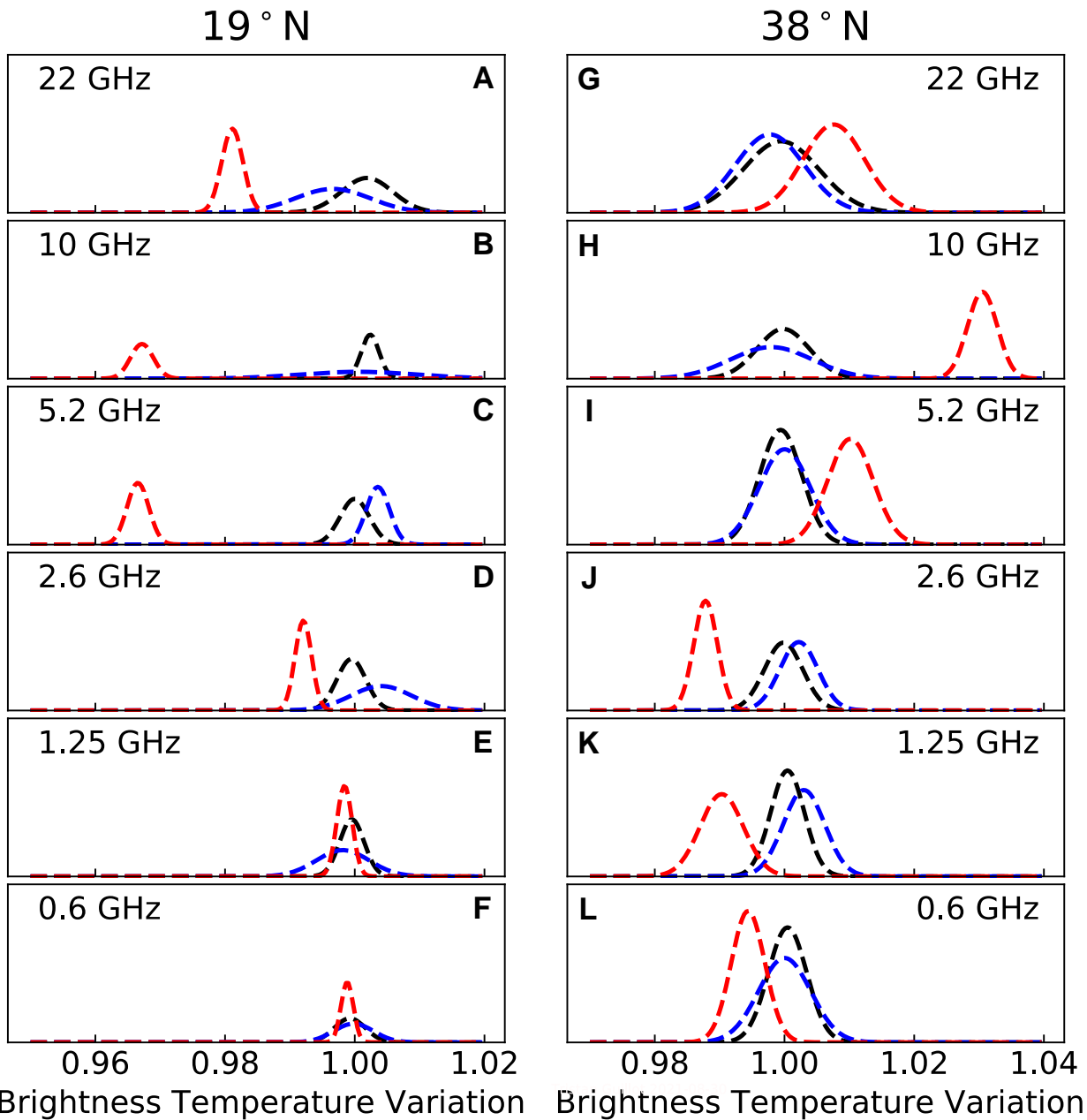


Figure S3. **Histogram of the brightness temperature variations measured inside and outside of the 19°N anticyclone (A-F) and 38°N cyclone (G-L).** The histograms correspond to brightness temperatures inside the feature (red bars), at similar latitudes but different longitudes (black bars) and at similar longitudes but different latitudes (blue bars). Gaussian models fitted to the histograms are shown as dashed curves. See table S5 for a list of the latitudes and longitudes used.

Fig. S4.

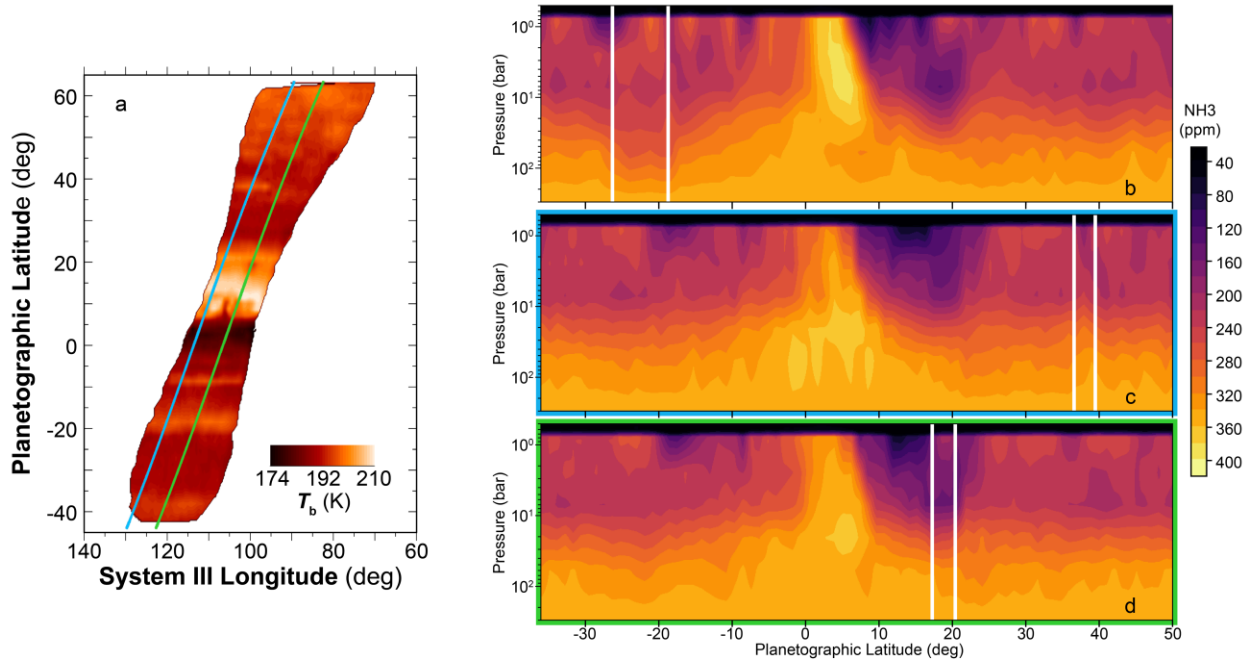


Figure S4. **Ammonia maps.** Panel (a): the same 10-GHz map as in Figure 1 and S1, with colored lines showing locations of latitudinal profiles for ammonia inversions. Panels (b-d): Ammonia maps assuming variations in T_b are due to opacity changes associated with ammonia (3,5). Implied changes in ammonia abundance associated with various meteorological features assumes all changes in T_b are due to opacity changes driven by ammonia variability. Panel (b): map corresponding to the 7th orbit that includes the GRS. Panel (c): map corresponding to the “blue” scan shown in panel (a), which includes the feature at 38°N. Panel (d): map corresponding to the “green” scan shown in panel (a), which includes the storm feature at 19°N.

Fig. S5.

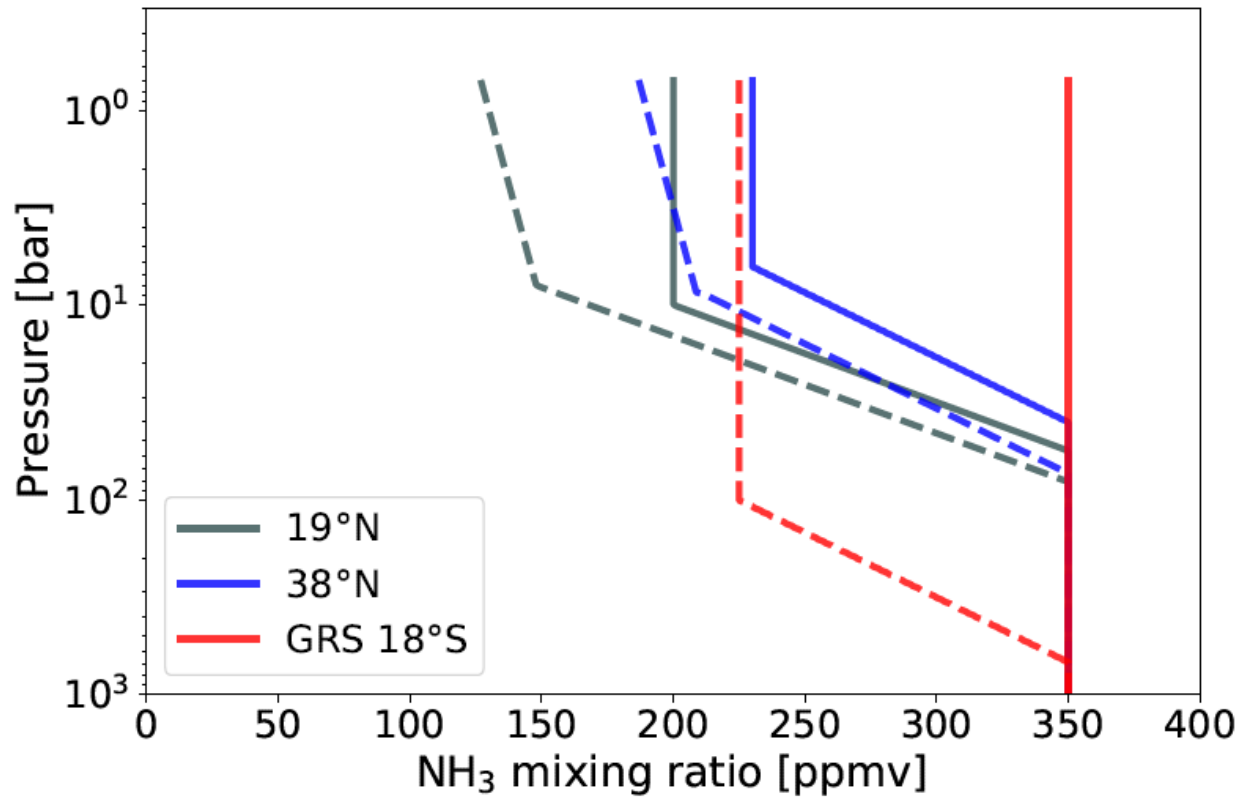


Figure S5. **Extreme NH_3 mixing ratios as a function of pressure obtained at latitudes 18°S , 19°N and 38°N .** The values account both for the atmosphere in the presence of vortexes and without these (Fig. S4). Solid lines indicate maximum values and dashed lines indicate minimum values.

Fig. S6.

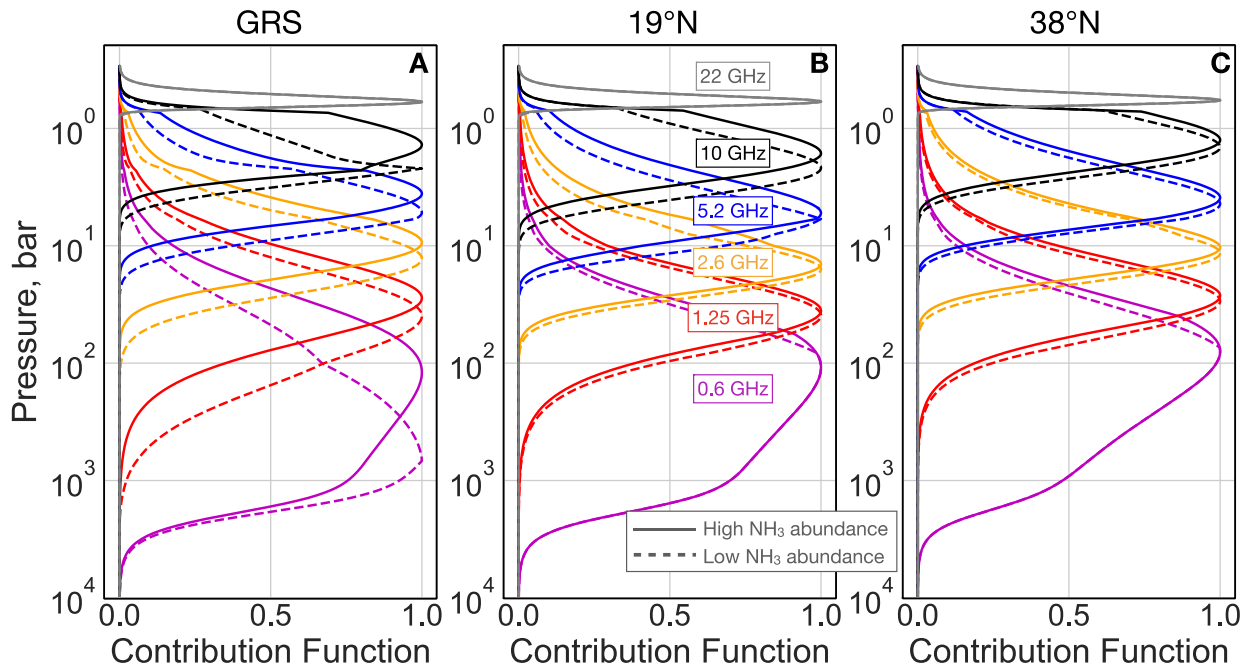


Figure S6. **MWR contribution functions for MWR observation frequencies.** Contribution functions for each vortex shown: the GRS (A), the 19°N anticyclone (B) and the 38°N cyclone (C). The contribution functions are adapted from a standard Jovian atmospheric model (2), to account for the varying ammonia profiles and viewing geometries, for each MWR frequencies: 0.6, 1.25, 2.6, 5.2, 10 and 22 GHz (from bottom to top, as labelled). The solid lines correspond to the highest NH_3 abundance fitting the measured brightness temperatures at those locations, dashed lines correspond to lowest NH_3 abundance fitting measured brightness temperatures.

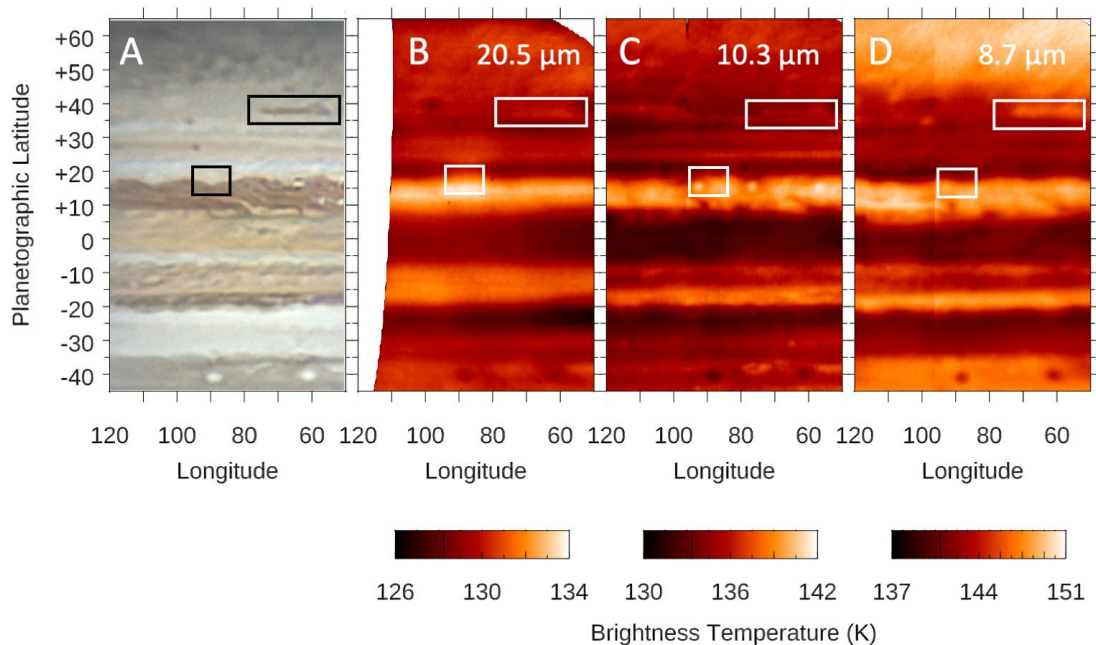


Figure S7. **Maps of the 19°N and 38°N features made in late May of 2019.** Panel A shows a color composite map of Jupiter (40) made on May 29, showing the positions of the compact feature at 19°N identified by the small rectangle and the more extended dark feature at 38°N identified by the larger rectangle. Panels B-D display maps of brightness temperatures at each of the filters whose central wavelengths are also shown; they were created from images made at the Subaru Telescope with the Cooled Mid-Infrared Camera / Spectrometer (COMICS) instrument from May 26 (41). The rectangles identifying the features in panel A are repeated in panels B-D in identical locations.

Table S1. Median T_b , T_b variation and residual for the anticyclone at 19°N vs. MWR frequency

Frequency	T_b	$\Delta T_b/T_b$	$\Delta T_b/T_b$ uncertainty
22 GHz	141.7 K	-0.0208	0.0026
10 GHz	198.6 K	-0.0352	0.0022
5.2 GHz	262.7 K	-0.0334	0.0028
2.6 GHz	344.3 K	-0.0074	0.0026
1.25 GHz	465.4 K	-0.0011	0.0022
0.6 GHz	856.0 K	-0.0004	0.0026

Table S2. Median brightness temperature, brightness temperature variation and residual for the anticyclone at 38°N vs. MWR frequency.

Frequency	T_b	$\Delta T_b/T_b$	$\Delta T_b/T_b$ uncertainty
22 GHz	140.9 K	0.0099	0.0072
10 GHz	189.3 K	0.0325	0.0067
5.2 GHz	246.9 K	0.0101	0.0053
2.6 GHz	331.6 K	-0.0144	0.0035
1.25 GHz	463.3 K	-0.0127	0.0046
0.6 GHz	861.8 K	-0.0056	0.0048

Table S3. Median brightness temperature, brightness temperature variation and residual for the GRS at 18.2°S vs. MWR frequency.

Frequency	T_b	$\Delta T_b/T_b$	$\Delta T_b/T_b$ uncertainty
22 GHz	139.8 K	-0.0132	0.0102
10 GHz	190.0 K	-0.0183	0.0118
5.2 GHz	244.8 K	-0.0122	0.0072
2.6 GHz	329.7 K	-0.0140	0.0024
1.25 GHz	460.9 K	0.0083	0.0021
0.6 GHz	857.7 K	0.0256	0.0025

Table S4: Range of parameters chosen for the Monte-Carlo calculations

Parameter	GRS	19°N	38°N
a	[-0.1,0.0]	[-0.1,0.0]	[0.0,0.1]
b	[0.0,0.2]	[-0.05,0.05]	[-0.1,0.0]
x_0	[-1,0]		
x_1	[0,1.2]		
x_2	[0.5,3.0]		
$\text{Log}_{10}\alpha_0$	[0,2]		
$\text{Log}_{10}\alpha_1$	[0,2]		
$\text{Log}_{10}\alpha_2$	[0,2]		

Table S5: Latitude and longitude ranges used for the brightness temperature histograms shown in Figure S3.

VORTEX	Latitudes	Longitudes	Line Color
19°N anticyclone	18.5°N, 20°N	99°W, 100.1°W	Red: inside vortex
19°N anticyclone	18.5°N, 20°N	102.5°W, 105°W	Black: similar latitudes, different longitudes
19°N anticyclone	15°N-17°N, 21-25°N	99°W, 100.1°W	Blue: similar longitudes different latitudes
38°N cyclone	37°N, 38°N	97°W, 103°W	Red: inside vortex
38°N cyclone	37°N, 38°N	85°W, 95°W	Black: similar latitudes, different longitudes
38°N cyclone	34°N-36°N, 40-43°N	97°W, 103°W	Blue: similar longitudes different latitudes

References and Notes

1. H. B. Niemann, S. K. Atreya, G. R. Carignan, T. M. Donahue, J. A. Haberman, D. N. Harpold, R. E. Hartle, D. M. Hunten, W. T. Kasprzak, P. R. Mahaffy, T. C. Owen, S. H. Way, The composition of the Jovian atmosphere as determined by the Galileo probe mass spectrometer. *J. Geophys. Res.* **103** (E10), 22831–22845 (1998). [doi:10.1029/98JE01050](https://doi.org/10.1029/98JE01050) [Medline](#)
2. S. J. Bolton, A. Adriani, V. Adumitroaie, M. Allison, J. Anderson, S. Atreya, J. Bloxham, S. Brown, J. E. P. Connerney, E. DeJong, W. Folkner, D. Gautier, D. Grassi, S. Gulkis, T. Guillot, C. Hansen, W. B. Hubbard, L. Iess, A. Ingersoll, M. Janssen, J. Jorgensen, Y. Kaspi, S. M. Levin, C. Li, J. Lunine, Y. Miguel, A. Mura, G. Orton, T. Owen, M. Ravine, E. Smith, P. Steffes, E. Stone, D. Stevenson, R. Thorne, J. Waite, D. Durante, R. W. Ebert, T. K. Greathouse, V. Hue, M. Parisi, J. R. Szalay, R. Wilson, Jupiter's interior and deep atmosphere: The initial pole-to-pole passes with the Juno spacecraft. *Science* **356**, 821–825 (2017). [doi:10.1126/science.aal2108](https://doi.org/10.1126/science.aal2108) [Medline](#)
3. C. Li, A. Ingersoll, M. Janssen, S. Levin, S. Bolton, V. Adumitroaie, M. Allison, J. Arballo, A. Bellotti, S. Brown, S. Ewald, L. Jewell, S. Misra, G. Orton, F. Oyafuso, P. Steffes, R. Williamson, The distribution of ammonia on Jupiter from a preliminary inversion of Juno microwave radiometer data. *Geophys. Res. Lett.* **44**, 5317–5325 (2017). [doi:10.1002/2017GL073159](https://doi.org/10.1002/2017GL073159)
4. A. P. Ingersoll, V. Adumitroaie, M. D. Allison, S. Atreya, A. A. Bellotti, S. J. Bolton, S. T. Brown, S. Gulkis, M. A. Janssen, S. M. Levin, C. Li, L. Li, J. I. Lunine, G. S. Orton, F. A. Oyafuso, P. G. Steffes, Implications of the ammonia distribution on Jupiter from 1 to 100 bars as measured by the Juno microwave radiometer. *Geophys. Res. Lett.* **44**, 7676–7685 (2017). [doi:10.1002/2017GL074277](https://doi.org/10.1002/2017GL074277) [Medline](#)
5. Y. Kaspi, E. Galanti, W. B. Hubbard, D. J. Stevenson, S. J. Bolton, L. Iess, T. Guillot, J. Bloxham, J. E. P. Connerney, H. Cao, D. Durante, W. M. Folkner, R. Helled, A. P. Ingersoll, S. M. Levin, J. I. Lunine, Y. Miguel, B. Militzer, M. Parisi, S. M. Wahl, Jupiter's atmospheric jet streams extend thousands of kilometres deep. *Nature* **555**, 223–226 (2018). [doi:10.1038/nature25793](https://doi.org/10.1038/nature25793) [Medline](#)
6. T. Guillot, Y. Miguel, B. Militzer, W. B. Hubbard, Y. Kaspi, E. Galanti, H. Cao, R. Helled, S. M. Wahl, L. Iess, W. M. Folkner, D. J. Stevenson, J. I. Lunine, D. R. Reese, A. Biekman, M. Parisi, D. Durante, J. E. P. Connerney, S. M. Levin, S. J. Bolton, A suppression of differential rotation in Jupiter's deep interior. *Nature* **555**, 227–230 (2018). [doi:10.1038/nature25775](https://doi.org/10.1038/nature25775) [Medline](#)
7. M. A. Janssen, J. E. Oswald, S. T. Brown, S. Gulkis, S. M. Levin, S. J. Bolton, M. D. Allison, S. K. Atreya, D. Gautier, A. P. Ingersoll, J. I. Lunine, G. S. Orton, T. C. Owen, P. G. Steffes, V. Adumitroaie, A. Bellotti, L. A. Jewell, C. Li, L. Li, S. Misra, F. A. Oyafuso, D. Santos-Costa, E. Sarkissian, R. Williamson, J. K. Arballo, A. Kitiyakara, A. Ulloa-Severino, J. C. Chen, F. W. Maiwald, A. S. Sahakian, P. J. Pingree, K. A. Lee, A. S. Mazer, R. Redick, R. E. Hodges, R. C. Hughes, G. Bedrosian, D. E. Dawson, W. A. Hatch, D. S. Russell, N. F. Chamberlain, M. S. Zawadski, B. Khayatian, B. R. Franklin, H. A. Conley, J. G. Kempenaar, M. S. Loo, E. T. Sunada, V. Vorperion, C. C. Wang,

MWR: Microwave radiometer for the Juno mission to Jupiter. *Space Sci. Rev.* **213**, 139–185 (2017). [doi:10.1007/s11214-017-0349-5](https://doi.org/10.1007/s11214-017-0349-5)

8. Materials and methods are available as supplementary materials.

9. F. Oyafuso, S. Levin, G. Orton, S. T. Brown, V. Adumitroaie, M. Janssen, M. H. Wong, L. N. Fletcher, P. Steffes, C. Li, S. Gulkis, S. Atreya, S. Misra, S. Bolton, Angular dependence and spatial distribution of Jupiter's centimeter-wave thermal emission from Juno's microwave radiometer. *Earth Space Sci.* **7**, e2020EA001254 (2020). [doi:10.1029/2020EA001254](https://doi.org/10.1029/2020EA001254)
10. I. de Pater, R. J. Sault, B. Butler, D. DeBoer, M. H. Wong, Peering through Jupiter's clouds with radio spectral imaging. *Science* **352**, 1198–1201 (2016). [doi:10.1126/science.aaf2210](https://doi.org/10.1126/science.aaf2210) [Medline](#)
11. I. de Pater, R. J. Sault, M. H. Wong, L. N. Fletcher, D. DeBoer, B. Butler, Jupiter's ammonia distribution derived from VLA maps at 3–37 GHz. *Icarus* **322**, 168–191 (2019). [doi:10.1016/j.icarus.2018.11.024](https://doi.org/10.1016/j.icarus.2018.11.024)
12. R. J. Terrile, R. F. Beebe, Summary of historical data: Interpretation of the pioneer and voyager cloud configurations in a time-dependent framework. *Science* **204**, 948–951 (1979). [doi:10.1126/science.204.4396.948](https://doi.org/10.1126/science.204.4396.948) [Medline](#)
13. M. H. Wong, A. A. Simon, J. W. Tollefson, I. de Pater, M. N. Barnett, A. I. Hsu, A. Stephens, G. S. Orton, S. W. Fleming, C. Goullaud, W. Januszewski, A. Roman, G. L. Bjoraker, S. K. Atreya, A. Adriani, L. Fletcher, High-resolution UV/optical/IR imaging of Jupiter in 2016–2019. *Astrophys. J. Suppl. Ser.* **247**, 58 (2020). [doi:10.3847/1538-4365/ab775f](https://doi.org/10.3847/1538-4365/ab775f)
14. R. S. Giles, L. N. Fletcher, P. G. J. Irwin, Cloud structure and composition of Jupiter's troposphere from 5- μ m Cassini VIMS spectroscopy. *Icarus* **257**, 457–470 (2015). [doi:10.1016/j.icarus.2015.05.030](https://doi.org/10.1016/j.icarus.2015.05.030)
15. A. R. Vasavada, A. P. Showman, Jovian atmospheric dynamics: An update after Galileo and Cassini. *Rep. Prog. Phys.* **68**, 1935–1996 (2005). [doi:10.1088/0034-4885/68/8/R06](https://doi.org/10.1088/0034-4885/68/8/R06)
16. A. F. Cheng, A. A. Simon-Miller, H. A. Weaver, K. H. Baines, G. S. Orton, P. A. Yanamandra-Fisher, O. Mousis, E. Pantin, L. Vanzi, L. N. Fletcher, J. R. Spencer, S. A. Stern, J. T. Clarke, M. J. Mutchler, K. S. Noll, Changing characteristics of Jupiter's Little Red Spot. *Astron. J.* **135**, 2446–2452 (2011). [doi:10.1088/0004-6256/135/6/2446](https://doi.org/10.1088/0004-6256/135/6/2446)
17. P. Marcus, Vortex dynamics in a shearing zonal flow. *J. Fluid Mech.* **215**, 393–430 (1990). [doi:10.1017/S0022112090002695](https://doi.org/10.1017/S0022112090002695)
18. P. S. Marcus, S. Pei, C.-H. Jiang, P. Hassanzadeh, Three-dimensional vortices generated by self-replication in stably stratified rotating shear flows. *Phys. Rev. Lett.* **111**, 084501 (2013). [doi:10.1103/PhysRevLett.111.084501](https://doi.org/10.1103/PhysRevLett.111.084501) [Medline](#)
19. M. H. Wong, I. de Pater, X. Asay-Davis, P. S. Marcus, C. Y. Go, Vertical structure of Jupiter's Oval BA before and after it reddened: What changed? *Icarus* **215**, 211–225 (2011). [doi:10.1016/j.icarus.2011.06.032](https://doi.org/10.1016/j.icarus.2011.06.032)

20. I. de Pater, M. H. Wong, P. Marcus, S. Luszcz-Cook, M. Ádámkóvics, A. Conrad, X. Asay-Davis, C. Go; de Pater et al, Persistent Rings in and around Jupiter's Anticyclones - Observations and Theory. *Icarus* **210**, 742–762 (2010). [doi:10.1016/j.icarus.2010.07.027](https://doi.org/10.1016/j.icarus.2010.07.027)
21. B. M. Peek, *The Planet Jupiter*, Faber and Faber, London, 1958.
22. M. Parisi *et al.*, The depth of Jupiter's Great Red Spot constrained by the Juno gravity overflights. *Science*.
23. T. Guillot, D. J. Stevenson, S. K. Atreya, S. J. Bolton, H. N. Becker, Storms and the depletion of ammonia in Jupiter: I. Microphysics of "Mushballs". *J. Geophys. Res. Planets* **125**, e2020JE006403 (2020). [doi:10.1029/2020JE006403](https://doi.org/10.1029/2020JE006403)
24. T. Guillot, C. Li, S. J. Bolton, S. T. Brown, A. P. Ingersoll, M. A. Janssen, S. M. Levin, J. I. Lunine, G. S. Orton, P. G. Steffes, D. J. Stevenson, Storms and the depletion of ammonia in Jupiter: II. Explaining the Juno observations. *J. Geophys. Res. Planets* **125**, e2020JE006404 (2020). [doi:10.1029/2020JE006404](https://doi.org/10.1029/2020JE006404)
25. M. Flasar, B. J. Conrath, J. A. Pirraglia, P. C. Clark, R. G. French, P. J. Gierasch, Thermal structure and dynamics of the Jovian Atmosphere I. The Great Red Spot. *J. Geophys. Res.* **86** (A10), 8759–8767 (1981). [doi:10.1029/JA086iA10p08759](https://doi.org/10.1029/JA086iA10p08759)
26. M. D. Prater, T. B. Sanford, A meddy off Cape St. Vincent. Part I: Description. *J. Phys. Oceanogr.* **24**, 1572–1586 (1994). [doi:10.1175/1520-0485\(1994\)024<1572:AMOCV>2.0.CO;2](https://doi.org/10.1175/1520-0485(1994)024<1572:AMOCV>2.0.CO;2)
27. O. Aubert, M. Le Bars, P. Le Gal, P. S. Marcus, The universal aspect ratio of vortices in rotating stratified flows: Experiments and observations. *J. Fluid Mech.* **706**, 34–45 (2012). [doi:10.1017/jfm.2012.176](https://doi.org/10.1017/jfm.2012.176)
28. P. Hassanzadeh, P. S. Marcus, P. Le Gal, The universal aspect ratio of vortices in rotating stratified flows: Theory and simulation. *J. Fluid Mech.* **706**, 46–57 (2012). [doi:10.1017/jfm.2012.180](https://doi.org/10.1017/jfm.2012.180)
29. D. Lemasquerier, G. Facchini, B. Favier, M. Le Bars, Remote determination of the shape of Jupiter's vortices from laboratory experiments. *Nat. Phys.* **16**, 695–700 (2020). [doi:10.1038/s41567-020-0833-9](https://doi.org/10.1038/s41567-020-0833-9) [Medline](#)
30. G. Heimpel, T. Gastine, J. Wicht, Wicht, Simulation of deep-seated zonal jets and shallow vortices in gas giant atmospheres. *Nat. Geosci.* **9**, 19–23 (2016). [doi:10.1038/ngeo2601](https://doi.org/10.1038/ngeo2601)
31. R. K. Yadav, M. Heimpel, J. Bloxham, Deep convection-driven vortex formation on Jupiter and Saturn. *Sci. Adv.* **6**, eabb9298 (2020). [doi:10.1126/sciadv.abb9298](https://doi.org/10.1126/sciadv.abb9298) [Medline](#)
32. M. Allison, Planetary Waves in Jupiter's equatorial atmosphere. *Icarus* **83**, 282–307 (1990). [doi:10.1016/0019-1035\(90\)90069-L](https://doi.org/10.1016/0019-1035(90)90069-L)
33. H. N. Becker, J. W. Alexander, S. K. Atreya, S. J. Bolton, M. J. Brennan, S. T. Brown, A. Guillaume, T. Guillot, A. P. Ingersoll, S. M. Levin, J. I. Lunine, Y. S. Aglyamov, P. G. Steffes, Small lightning flashes from shallow electrical storms on Jupiter. *Nature* **584**, 55–58 (2020). [doi:10.1038/s41586-020-2532-1](https://doi.org/10.1038/s41586-020-2532-1) [Medline](#)
34. M. Wong, 2017. Wide Field Coverage for Juno (WFCJ). Mikulski Archive for Space Telescopes (2021). [doi:10.17909/T94T1H](https://doi.org/10.17909/T94T1H).

35. S. Bolton *et al.*, Microwave observations constrain the Depth of vortices in Jupiter's atmosphere. Zenodo doi:[10.5281/zenodo.5527240](https://doi.org/10.5281/zenodo.5527240).
36. A. J. Dessler, Coordinate systems, in *Physics of the Jovian Magnetosphere*, A. J. Dessler, Ed. Cambridge University Press, pp. 498-504, Cambridge University Press, 1983.
37. A. Bellotti, Jupiter: A study of atmospheric composition, structure and dynamics using microwave techniques. Ph.D. Thesis, Georgia Institute of Technology (2018).
38. C. Palotai, T. E. Dowling, L. N. Fletcher, 3D modeling of interactions between Jupiter's ammonia clouds and large anticyclones. *Icarus* **232**, 141–156 (2014).
[doi:10.1016/j.icarus.2014.01.005](https://doi.org/10.1016/j.icarus.2014.01.005)
39. J. H. Rogers, Jupiter in 2019, British Astronomical Association Interim Report 4 (2019);
https://britastro.org/sites/default/files/JupLet%202019cc_Report-no4.pdf;
https://britastro.org/sites/default/files/Report-no4_Figures.pdf.
40. M. Vedovato, L.-L. Dauvergne, Association of Lunar and Planetary Observers (ALPO) – Japan: <https://alpo-j.sakura.ne.jp/kk19/j190529s.htm>, 2019 May 29.
41. H. Kataza *et al.*, In: S. Ikeuchi, Hearnshaw, J., Hanawa, T. (Eds.), *8th Asian-Pacific Regional Meeting, vol. II*, pp. 17-18 (2002).